PHYSICAL REVIEW D **110,** 034036 (2024)

Extraction of transhelicity worm-gear distributions and opportunities at the Electron-Ion Collider in China

Ke Yang,[1,*] Tianbo Liu,[2,3,†] Peng Sun,[4,5,‡] Yuxiang Zhao,[3,4,5,6,§] and Bo-Qiang Ma[1,7,8,‖]
[1]*School of Physics, Peking University, Beijing 100871, China*
[2]*Key Laboratory of Particle Physics and Particle Irradiation (MOE),*
Institute of Frontier and Interdisciplinary Science, Shandong University,
Qingdao, Shandong 266237, China
[3]*Southern Center for Nuclear-Science Theory (SCNT), Institute of Modern Physics,*
Chinese Academy of Sciences, Huizhou 516000, China
[4]*Institute of Modern Physics, Chinese Academy of Sciences, Lanzhou, Gansu Province 730000, China*
[5]*University of Chinese Academy of Sciences, Beijing 100049, China*
[6]*Key Laboratory of Quark and Lepton Physics (MOE) and Institute of Particle Physics,*
Central China Normal University, Wuhan 430079, China
[7]*Center for High Energy Physics, Peking University, Beijing 100871, China*
[8]*Collaborative Innovation Center of Quantum Matter, Beijing, China*

(Received 26 March 2024; accepted 6 August 2024; published 29 August 2024)

We present a global analysis of the transhelicity worm-gear distribution function, $g_{1T}^{\perp}$, by fitting the longitudinal-transverse double-spin asymmetry data of the semi-inclusive deep inelastic scattering. The analysis is performed within the framework of transverse momentum dependent factorization and evolution. It is found that the u-quark favors a positive distribution and the d-quark favors a negative distribution, which is consistent with previous model calculations and phenomenological extractions. Based on the fit to existing world data, we also study the impact of the proposed Electron-Ion Collider in China and conclude that it can significantly improve the precision of the worm-gear distribution function and hence enhance our understanding of nucleon spin structures.

DOI: 10.1103/PhysRevD.110.034036

I. INTRODUCTION

Understanding the internal structure of nucleons is pivotal for comprehending the strong force that binds quarks and gluons within nucleons, and for shedding light on the fundamental properties of the matter. In recent years, the pursuit of multidimensional tomography of the nucleon has emerged as a cutting-edge approach to probe distributions of quarks and gluons within the nucleon, offering a deeper understanding of its internal dynamics. Transverse momentum dependent (TMD) parton distribution functions (PDFs) contain the information of the parton transverse momentum with respect to the parent nucleon, and hence provide three-dimensional imaging of the nucleon in the momentum space.

At the leading twist, there are eight TMDs for quarks [1–4]. Among them, the worm-gear-T distribution $g_{1T}^{\perp}(x, k_T^2)$, also known as the transhelicity distribution [5,6] or the Kotzinian-Mulders function [7,8], describes the probability density of finding a longitudinally polarized quark with longitudinal momentum fraction x and transverse momentum k_T in a transversely polarized nucleon. As well as the worm-gear-L, or longi-transversity, distribution $h_{1L}^{\perp}$ that describes the probability density of finding a transversely polarized quark in a longitudinally polarized nucleon, it can be expressed as the overlap between wave functions differing by one unit of orbital angular momentum [9–13], and many efforts have been devoted to the worm-gear TMDs to understand nucleon spin and flavor structures.

Although the two worm-gear distributions are defined as independent quantities from the decomposition of the quark-quark correlator, some relation, such as $g_{1T}^{\perp} = -h_{1L}^{\perp}$, is suggested based on quark model-like calculations [5,6,11,14–16]. Following the SU(6) spin-flavor structure, the $g_{1T}^{\perp}$ distribution of the up quark was predicted to be positive and with a greater magnitude than the negative

---

[*] Contact author: yangke2020@stu.pku.edu.cn
[†] Contact author: liutb@sdu.edu.cn
[‡] Contact author: pengsun@impcas.ac.cn
[§] Contact author: yxzhao@impcas.ac.cn
[‖] Contact author: mabq@pku.edu.cn

down-quark distribution, and explicit calculations have been done in the light cone constituent quark model [11,17–20], the spectator diquark model [10,14,20,21], the MIT bag model [16], and the covariant parton model [15]. On the other hand, the large-N_c approximation [22] states that the worm-gear distributions of up quark and down quark only differ by a sign and have the same magnitude, *i.e.,* $g_{1T}^{\perp u} = -g_{1T}^{\perp d}$. Besides, if taking the Wandzura-Wilczek (WW)-type approximation [7,8,23–26], which neglects the contribution from quark-gluon-quark correlations, one may relate the transhelicity worm-gear distribution to the helicity distribution as

$$g_{1T}^{\perp(1)}(x) \overset{\text{WW}}{\approx} x \int_x^1 \frac{dy}{y} g_1(y), \tag{1}$$

where

$$g_{1T}^{\perp(1)}(x) \equiv \pi \int dk_T^2 \frac{k_T^2}{2M^2} g_{1T}^{\perp}(x, k_T^2), \tag{2}$$

is the first transverse moment that has also been studied in lattice QCD [27–29].

In experiment, the semi-inclusive deep inelastic scattering (SIDIS) is one of the main processes to study TMDs. According to the TMD factorization, the transhelicity distribution $g_{1T}^{\perp}$ contributes to a double spin asymmetry A_{LT} with azimuthal modulation as $\cos(\phi_h - \phi_S)$. With the development of polarized beams and targets, this asymmetry has been measured by HERMES [30], COMPASS [31–33], and Jefferson Lab (JLab) [34]. In some recent phenomenological analyses [35,36], it was found that the extracted worm-gear distributions supported the positive result for the up quark and the negative result for the down quark as suggested by the model calculations. However, due to the limited accuracy of existing world data, one has to introduce some bias in the fit to obtain reasonable results and almost no constraint is put on sea quarks.

The Electron-Ion Collider in China (EicC) is proposed as a future facility in nuclear physics, and one of its main physics goals is to precisely measure nucleon TMDs via the SIDIS process. It is designed to deliver a 3.5 GeV electron beam with 80% polarization colliding with various types of ion beams. The designed energy of the proton beam is 20 GeV and correspondingly the energy of the ^{3}He beam is 40 GeV. Both the proton and the ^{3}He beams can be longitudinally or transversely polarized with 70% polarization. The instantaneous luminosity can reach about 2×10^{33} cm^{-2} s^{-1}. The EicC kinematic coverage will fill the gap between multihall SIDIS program at the 12 GeV upgraded JLab, which covers relatively large-x region dominated by valence quarks, and the Electron-Ion Collider (EIC) to be built at the Brookhaven National Laboratory (BNL), which can reach the small-x region down to about 10^{-4} [37,38]. Therefore, a combination of all these facilities is expected to provide precise determination of TMDs in a full kinematic coverage [39], towards a complete three-dimensional imaging of nucleon spin structures.

In this paper, we perform a global analysis of transhelicity TMDs by fitting the longitudinal-transverse double spin asymmetry data from HERMES, COMPASS, and JLab. Taking the world data fit result as the baseline, we further study the impact of the EicC SIDIS program on the determination of the worm-gear distribution. The rest of the paper is organized as follows. In Sec. II, we briefly review the theoretical framework. In Sec. III, we present the parametrization of the transhelicity worm-gear distributions and the fit results to world data. In Sec. IV, we study the EicC impact on the extraction of the worm-gear distributions by adding simulated pseudodata in the fit. A summary is drawn in Sec. V.

II. THEORETICAL FORMALISM

We consider the SIDIS process,

$$\ell(l) + N(P) \longrightarrow \ell(l') + h(P_h) + X, \tag{3}$$

where ℓ represents the lepton, N represents the nucleon, and h represents the detected hadron. The four-momenta of corresponding particles are given in parentheses. The commonly used kinematic variables for the SIDIS process are defined as

$$Q^2 = -(l - l')^2 = -q^2, \tag{4}$$

$$x = \frac{Q^2}{2P \cdot q}, \qquad y = \frac{P \cdot q}{P \cdot l}, \qquad z = \frac{P \cdot P_h}{P \cdot q}, \tag{5}$$

$$\gamma = \frac{2xM}{Q} = \frac{MQ}{P \cdot q}, \tag{6}$$

where $q = l - l'$ is the transferred momentum and M is the nucleon mass.

For the SIDIS process with a transversely polarized target and a longitudinally polarized lepton beam, one can write the differential cross section within the one-photon-exchange approximation as [40]

$$\begin{aligned}
&\frac{d\sigma}{dx dy dz d\phi_h d\phi_S dP_{hT}^2} \\
&= \sigma_0 \Big\{ F_{UU} + \lambda_e |S_\perp| \Big[\sqrt{1-\varepsilon^2} \cos(\phi_h - \phi_S) F_{LT}^{\cos(\phi_h - \phi_S)} \\
&\quad + \sqrt{2\varepsilon(1-\varepsilon)} \cos(2\phi_h - \phi_S) F_{LT}^{\cos(2\phi_h - \phi_S)} \\
&\quad + \sqrt{2\varepsilon(1-\varepsilon)} \cos(\phi_S) F_{LT}^{\cos\phi_S} + \cdots \Big] \Big\},
\end{aligned} \tag{7}$$

where

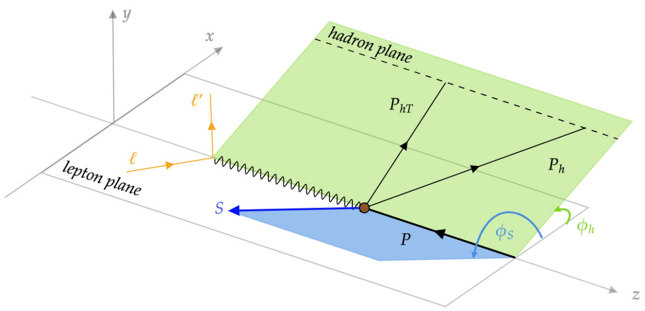

FIG. 1. Trento conventions of the transverse momentum and azimuthal angles.

$$\sigma_0 = \frac{\alpha^2}{xyQ^2}\frac{y^2}{2(1-\varepsilon)}\left(1+\frac{\gamma^2}{2x}\right), \tag{8}$$

α is the electromagnetic fine structure constant, $|S_\perp|$ represents the transversal component of the nucleon spin vector, λ_e represents the helicity of the lepton beam, and ε is the ratio of longitudinal and transverse photon flux,

$$\varepsilon = \frac{1-y-\frac{1}{4}\gamma^2y^2}{1-y+\frac{1}{2}y^2+\frac{1}{4}\gamma^2y^2}. \tag{9}$$

As shown in Fig. 1, we follow the Trento conventions [41], in which the momenta of the virtual photon and the nucleon are chosen along the $\hat{z}$ direction. One can express the transverse momentum P_{hT} of the hadron and the azimuthal angles ϕ_h and ϕ_S in Lorentz invariant forms as

$$P_{hT} = \sqrt{-g_\perp^{\mu\nu}P_{h\mu}P_{h\nu}}, \tag{10}$$

$$\cos\phi_h = -\frac{l_\mu P_{h\nu}g_\perp^{\mu\nu}}{l_\perp P_{hT}}, \qquad \sin\phi_h = -\frac{l_\mu P_{h\nu}\epsilon_\perp^{\mu\nu}}{l_\perp P_{hT}}, \tag{11}$$

$$\cos\phi_S = -\frac{l_\mu S_{\perp\nu}g_\perp^{\mu\nu}}{l_\perp S_\perp}, \qquad \sin\phi_S = -\frac{l_\mu S_{\perp\nu}\epsilon_\perp^{\mu\nu}}{l_\perp S_\perp}, \tag{12}$$

where $l_\perp = \sqrt{-g_\perp^{\mu\nu}l_\mu l_\nu}$ and $S_\perp = \sqrt{-g_\perp^{\mu\nu}S_\mu S_\nu}$ with S^μ being the spin vector of the nucleon. The transverse metric and the transverse antisymmetry tensor are defined as

$$g_\perp^{\mu\nu} = g^{\mu\nu} - \frac{q^\mu P^\nu + P^\mu q^\nu}{P\cdot q(1+\gamma^2)} + \frac{\gamma^2}{1+\gamma^2}\left(\frac{q^\mu q^\nu}{Q^2} - \frac{P^\mu P^\nu}{M^2}\right), \tag{13}$$

$$\epsilon_\perp^{\mu\nu} = \epsilon^{\mu\nu\rho\sigma}\frac{P_\rho q_\sigma}{P\cdot q\sqrt{1+\gamma^2}}, \tag{14}$$

where $\epsilon^{\mu\nu\rho\sigma}$ is the totally antisymmetric tensor with the convention $\epsilon^{0123} = 1$.

The worm-gear distribution $g_{1T}^\perp$ can be extracted from the longitudinal-transverse double spin asymmetry, which is given by the ratio between the structure functions $F_{LT}^{\cos(\phi_h-\phi_S)}$ and F_{UU}. According to the TMD factorization [40], the structure functions at low transverse momentum, i.e., small $\delta = |P_{hT}|/(zQ)$, can be approximated in terms of TMD PDF and TMD fragmentation function (FF) as

$$F_{UU} = |C_V(Q^2,\mu)|^2 x\sum_q e_q^2\int_0^\infty \frac{b_T db_T}{2\pi}J_0\left(\frac{b_T P_{hT}}{z}\right) \times f_{1,q\leftarrow H}(x,b_T;\mu,\zeta)D_{1,q\rightarrow h}(z,b_T;\mu,\bar{\zeta}) + \mathcal{O}\left(\frac{P_{hT}^2}{Q^2}\right), \tag{15}$$

$$F_{LT}^{\cos(\phi_h-\phi_S)} = |C_V(Q^2,\mu)|^2 x\sum_q e_q^2 M\int_0^\infty \frac{b_T^2 db_T}{2\pi} \times J_1\left(\frac{b_T P_{hT}}{z}\right)g_{1T,q\leftarrow H}^\perp(x,b_T;\mu,\zeta) \times D_{1,q\rightarrow h}(z,b_T;\mu,\bar{\zeta}) + \mathcal{O}\left(\frac{P_{hT}^2}{Q^2}\right), \tag{16}$$

where e_q is the electric charge of the quark with flavor q, C_V is the hard factor that can be calculated via perturbative QCD, and J_0 and J_1 are the first kind Bessel functions. Here the unpolarized TMD PDF f_1, the worm-gear TMD PDF $g_{1T}^\perp$, and the unpolarized TMD FF D_1 are given in b_T space. They are related to corresponding functions in the transverse momentum space through Fourier transforms,

$$f_1(x,k_T;\mu,\zeta) = \int_0^\infty \frac{b_T db_T}{2\pi}J_0(b_T k_T)f_1(x,b_T;\mu,\zeta), \tag{17}$$

$$\frac{k_T}{M}g_{1T}^\perp(x,k_T;\mu,\zeta) = \int_0^\infty \frac{b_T^2 db_T}{2\pi}MJ_1(b_T k_T)g_{1T}^\perp(x,b_T;\mu,\zeta), \tag{18}$$

$$D_1(z,p_T;\mu,\zeta) = \int_0^\infty \frac{b_T db_T}{2\pi}J_0(b_T p_T)D_1(z,b_T;\mu,\zeta), \tag{19}$$

where k_T represents the quark transverse momentum with respect to the nucleon and p_T represents the quark transverse momentum with respect to the produced hadron. The details of the Fourier transformation are given in Appendix A.

A. Evolution of TMD PDFs and FFs

The energy scale dependence on μ and ζ of the TMD functions are given by the evolution equations,

$$\mu^2\frac{d}{d\mu^2}F(x,b_T;\mu,\zeta) = \frac{\gamma_F(\mu,\zeta)}{2}F(x,b_T;\mu,\zeta), \tag{20}$$

$$\zeta \frac{d}{d\zeta} F(x, b_T; \mu, \zeta) = -\mathcal{D}(\mu, b_T) F(x, b_T; \mu, \zeta), \tag{21}$$

where γ_F is the anomalous dimension, and $\mathcal{D}$ is the rapidity anomalous dimension (RAD), also known as the Collins-Soper kernel. The F represents some TMD PDF or TMD FF, i.e., f_1, D_1, and $g_{1T}^{\perp}$ in this study. One may have the formal solution,

$$F(x, b_T; \mu, \zeta) = R[(b_T; \mu_i, \zeta_i) \to (b_T; \mu, \zeta)] F(x, b_T; \mu_i, \zeta_i), \tag{22}$$

which relates the TMD PDF (or FF) at (μ, ζ) to that at the initial point (μ_i, ζ_i). The evolution factor $R[(b_T; \mu_i, \zeta_i) \to (b_T; \mu, \zeta)]$ can be expressed as

$$R[(b_T; \mu_i, \zeta_i) \to (b_T; \mu, \zeta)] = \exp\left[\int_{\mathcal{P}} \left(\frac{\gamma_F(\mu, \zeta)}{\mu} d\mu - \frac{\mathcal{D}(\mu, b_T)}{\zeta} d\zeta\right)\right], \tag{23}$$

where $\mathcal{P}$ represents the path connecting the scales (μ_i, ζ_i) and (μ, ζ). As a common choice, we set the energy scales as $\mu^2 = \zeta = Q^2$.

According to the integrability condition [42]

$$\zeta \frac{d}{d\zeta} \gamma_F(\mu, \zeta) = -\mu \frac{d}{d\mu} \mathcal{D}(\mu, b_T) = -\Gamma_{\text{cusp}}(\mu), \tag{24}$$

the evolution factor $R[(b_T; \mu_i, \zeta_i) \to (b_T; Q, Q^2)]$ is in principle path independent. However, it differs from path to path when truncating at some fixed order in perturbation theory. As suggested in Ref. [43], the condition (24) allows one to construct a two-dimensional field $\mathcal{F}(\mu, \zeta)$, of which the gradient is given by $\mathbf{E} = (\gamma_F/2, -\mathcal{D})$. Then $F(x, b_T, \mu, \zeta)$ remains unchanged if the path is along the equipotential line of $\mathbf{E}$, referred to as a null-evolution line. In the (μ, ζ) plane, there is a unique saddle point (μ_0, ζ_0) defined by

$$\mathcal{D}(\mu_0, b_T) = 0, \qquad \gamma_F(\mu_0, \zeta_0) = 0. \tag{25}$$

Among the null-evolution lines, only the one passing through the saddle point has finite ζ at all values of μ. Hence, the $F(x, b_T) \equiv F(x, b_T; \mu_0, \zeta_0)$ is referred to as the optimal TMD PDF or FF [43]. Owing to the good properties of the null-evolution line and the saddle point, we firstly evolve the F from the saddle point along the null-evolution line to the point with $\mu = Q$; secondly, we evolve the F along the straight line keeping $\mu = Q$ fixed until reaching the point with $\zeta = Q^2$. The result for the evolution factor $R[(b_T; \mu_i, \zeta_i) \to (b_T; Q, Q^2)]$ along this path is [43]

$$R[(b_T; \mu_i, \zeta_i) \to (b_T; Q, Q^2)] = \left(\frac{Q^2}{\zeta_\mu(Q, b_T)}\right)^{-\mathcal{D}(Q, b_T)}. \tag{26}$$

TABLE I. Orders of perturbative calculations for anomalous dimensions and the $C(\mathbb{C})$ functions in the optimal TMD PDF and FF. The evolution factor in the calculation is at the next-to-next-to-leading-logarithmic (NNLL) accuracy.

	Γ_{cusp}	γ_V	$\mathcal{D}_{\text{resum}}$	ζ_μ^{pert}	ζ_μ^{exact}
R	α_s^3	α_s^2	α_s^2	α_s^1	α_s^1
	f_1	D_1	$g_{1T}^{\perp}$		
$C(\mathbb{C})$	α_s^1	α_s^1	α_s^0		

The expressions for $\mathcal{D}(Q, b_T)$ and $\zeta_\mu(Q, b_T)$ can be found in Appendix B. The precision for the perturbative calculation of various factors in powers of α_s in this work is summarized in Table I. Here we take the NNLL parametrization from the SV19 article, considering the existing asymmetry data are not accurate enough.

B. Unpolarized TMD PDF and FF

For unpolarized TMD PDFs and FFs, we adopt the SV19 parametrization [43]. The optimal unpolarized TMD PDF and FF are expressed as

$$f_{1,f\leftarrow h}(x, b_T) = \sum_{f'} \int_x^1 \frac{dy}{y} C_{f\leftarrow f'}\left(y, b_T, \mu_{\text{OPE}}^{\text{PDF}}\right) \times f_{1,f'\leftarrow h}\left(\frac{x}{y}, \mu_{\text{OPE}}^{\text{PDF}}\right) f_{\text{NP}}(x, b_T), \tag{27}$$

$$D_{1,f\to h}(z, b_T) = \frac{1}{z^2} \sum_{f'} \int_z^1 \frac{dy}{y} y^2 \mathbb{C}_{f\to f'}\left(y, b_T, \mu_{\text{OPE}}^{\text{FF}}\right) \times d_{1,f'\to h}\left(\frac{z}{y}, \mu_{\text{OPE}}^{\text{FF}}\right) D_{\text{NP}}(z, b_T), \tag{28}$$

where $f_{1,f'\leftarrow h}$ and $d_{1,f'\to h}$ are collinear PDFs and FFs. $f_1(x, \mu)$ $(D_1(z, \mu))$ is the collinear unpolarized PDF (FF) and we choose the NNPDF31 [44] (DSS [45–47]) parametrizations. The scales $\mu_{\text{OPE}}^{\text{PDE}}$ and $\mu_{\text{OPE}}^{\text{FF}}$ are chosen as

$$\mu_{\text{OPE}}^{\text{PDE}} = \frac{2e^{-\gamma_E}}{b_T} + 2\ \text{GeV}, \tag{29}$$

$$\mu_{\text{OPE}}^{\text{FF}} = \frac{2e^{-\gamma_E} z}{b_T} + 2\ \text{GeV}, \tag{30}$$

where γ_E is the Euler-Mascheroni constant. The 2 GeV shift is introduced to keep the PDFs and FFs in perturbative region when b_T is large. The nonperturbative functions $f_{\text{NP}}(x, b_T)$ and $D_{\text{NP}}(z, b_T)$ are to be parametrized.

For unpolarized TMD PDF, the coefficient function C can be written as

$$C_{f\leftarrow f'}(x,b_T,\mu)=\delta(1-x)\delta_{ff'}+a_s(\mu)\left(-\mathbf{L}_\mu P^{(1)}_{f\leftarrow f'}+C^{(1,0)}_{f\leftarrow f'}\right),\tag{31}$$

up to next-to-leading order (NLO), where $a_s=\frac{g^2(\mu)}{(4\pi)^2}$ and $g(\mu)$ is the QCD coupling constant. $\mathbf{L}_\mu$ is defined as

$$\mathbf{L}_\mu=\ln\left(\frac{b_T^2\mu^2}{4e^{-2\gamma_E}}\right).\tag{32}$$

$P^{(1)}_{f\leftarrow f'}$ is the coefficient of the PDF evolution kernel, which reads,

$$P^{(1)}_{q\leftarrow q'}(x)=2C_F\left(\frac{1+x^2}{1-x}\right)_+\delta_{qq'},\tag{33}$$

$$P^{(1)}_{q\leftarrow g}(x)=1-2x+2x^2.\tag{34}$$

The "+" prescription is defined as

$$\int_{x_0}^1 dx[g(x)]_+f(x)=\int_0^1 dxg(x)[f(x)\Theta(x-x_0)-f(1)],\tag{35}$$

where $\Theta(x-x_0)$ is the Heaviside step function. $C_F=4/3$ is the quadratic Casimir eigenvalue of the fundamental representation of $SU(3)$. The expressions of $C^{(n,0)}_{f\leftarrow f'}$ can be found in Ref. [48], and their NLO terms are

$$C^{(1,0)}_{q\leftarrow q'}(x)=C_F\left(2\bar{x}-\delta(\bar{x})\frac{\pi^2}{6}\right)\delta_{qq'},\tag{36}$$

$$C^{(1,0)}_{q\leftarrow g}(x)=2x\bar{x},\tag{37}$$

and $\bar{x}=1-x$.

For unpolarized TMD FF, one should replace $C_{f\leftarrow f'}(x,b_T,\mu)$, $P^{(1)}_{f\leftarrow f'}$ and $C^{(n,0)}_{f\leftarrow f'}(x)$ by $\mathbb{C}_{f\rightarrow f'}(z,b_T,\mu)$, $\mathbb{P}^{(1)}_{f\rightarrow f'}$, and $\mathbb{C}^{(n,0)}_{f\rightarrow f'}(z)$, which at NLO are expressed as

$$\mathbb{P}^{(1)}_{q\rightarrow q'}(z)=\frac{2C_F}{z^2}\left(\frac{1+z^2}{1-z}\right)_+\delta_{qq'},\tag{38}$$

$$\mathbb{P}^{(1)}_{q\rightarrow g}(z)=\frac{2C_F}{z^2}\frac{1+(1-z)^2}{z},\tag{39}$$

$$\mathbb{C}^{(1,0)}_{q\rightarrow q'}(z)=\frac{C_F}{z^2}\left[2(1-z)+\frac{4(1+z^2)\ln z}{1-z}\right.\tag{40}$$

$$\left.-\delta(1-z)\frac{\pi^2}{6}\right]\delta_{qq'},\tag{41}$$

$$\mathbb{C}^{(1,0)}_{q\rightarrow g}(z)=\frac{2C_F}{z^2}\left[z+2(1+(1-z)^2)\frac{\ln z}{z}\right].\tag{42}$$

C. Worm-gear asymmetry

The longitudinal-transverse double spin asymmetry of the SIDIS process is defined as

$$A_{LT}=\frac{1}{|S_\perp||\lambda_e|}\frac{[\mathrm{d}\sigma_{LT}(+,\uparrow)-\mathrm{d}\sigma_{LT}(-,\uparrow)]-[\mathrm{d}\sigma_{LT}(+,\downarrow)-\mathrm{d}\sigma_{LT}(-,\downarrow)]}{\mathrm{d}\sigma_{LT}(+,\uparrow)+\mathrm{d}\sigma_{LT}(-,\uparrow)+\mathrm{d}\sigma_{LT}(+,\downarrow)+\mathrm{d}\sigma_{LT}(-,\downarrow)},\tag{43}$$

where $+$ $(-)$ represents the positive (negative) helicity state of the electron beam and $\uparrow$ $(\downarrow)$ represents the transverse spin direction of nucleon $S_\perp$ to be parallel (antiparallel) to the designated positive transverse axis. The worm-gear asymmetry is defined as $\cos(\phi_h-\phi_S)$ modulation of the double spin asymmetry,

$$A_{LT}^{\cos(\phi_h-\phi_S)}=\frac{\langle 2\cos(\phi_h-\phi_S)\sigma_{\mathrm{LT}}\rangle}{\sqrt{1-\varepsilon^2}\langle\sigma_{UU}\rangle}=\frac{F_{LT}^{\cos(\phi_h-\phi_S)}}{F_{UU}}.\tag{44}$$

and one can express it with functions we defined above as

$$A_{LT}^{\cos(\phi_h-\phi_S)}=\frac{M\sum_q e_q^2\int_0^\infty\frac{b_T^2db_T}{2\pi}J_1\left(\frac{b_TP_{hT}}{z}\right)R^2[(b_T;\mu_i,\zeta_i)\rightarrow(b_T;Q,Q^2)]g^\perp_{1T,q\leftarrow N}(x,b_T)D_{1,q\rightarrow h}(z,b_T)}{\sum_q e_q^2\int_0^\infty\frac{b_Tdb_T}{2\pi}J_0\left(\frac{b_TP_{hT}}{z}\right)R^2[(b_T;\mu_i,\zeta_i)\rightarrow(b_T;Q,Q^2)]f_{1,q\leftarrow N}(x,b_T)D_{1,q\rightarrow h}(z,b_T)},\tag{45}$$

where N is the target and h is the detected hadron.

III. EXTRACTION OF THE WORM-GEAR DISTRIBUTIONS

With the formalism above, we perform a global analysis of world SIDIS data to extract the worm-gear distributions $g_{1T}^{\perp}$ of the nucleon. The results will also serve as the baseline for the impact study of the EicC.

We parametrize the optimal worm-gear distributions of the proton at the initial scale as

$$g_{1T,q\leftarrow p}^{\perp}(x,b_T) = N_q \frac{(1-x)^{\alpha_q} x^{\beta_q}}{\mathrm{B}(\alpha+1,\beta+1)} \exp\left(-r_q b_T^2\right) \tag{46}$$

for u and d quarks and

$$g_{1T,q\leftarrow p}^{\perp}(x,b_T) = N_q f_1(x,\mu_0) \exp\left(-r_q b_T^2\right) \tag{47}$$

for $\bar{u}$, $\bar{d}$, s, and $\bar{s}$ quarks with $\mu_0 = 2$ GeV. Here $\mathrm{B}(\alpha+1, \beta+1)$ is the Euler Beta function, introduced to reduce the correlation among parameters. Assuming the isospin symmetry, we can express corresponding distribution functions of the neutron as

$$g_{1T,u\leftarrow n}^{\perp}(x,b_T) = g_{1T,d\leftarrow p}^{\perp}(x,b_T), \tag{48}$$

$$g_{1T,\bar{u}\leftarrow n}^{\perp}(x,b_T) = g_{1T,\bar{d}\leftarrow p}^{\perp}(x,b_T), \tag{49}$$

$$g_{1T,d\leftarrow n}^{\perp}(x,b_T) = g_{1T,u\leftarrow p}^{\perp}(x,b_T), \tag{50}$$

$$g_{1T,\bar{d}\leftarrow n}^{\perp}(x,b_T) = g_{1T,\bar{u}\leftarrow p}^{\perp}(x,b_T), \tag{51}$$

$$g_{1T,s\leftarrow n}^{\perp}(x,b_T) = g_{1T,s\leftarrow p}^{\perp}(x,b_T), \tag{52}$$

$$g_{1T,\bar{s}\leftarrow n}^{\perp}(x,b_T) = g_{1T,\bar{s}\leftarrow p}^{\perp}(x,b_T). \tag{53}$$

TABLE II. The parameters for nonperturbative functions of the optimal unpolarized TMD PDF and FF. The units are in GeV^2 except that λ_4 is dimensionless.

λ_1	λ_2	λ_3	λ_4	λ_5
0.198	9.3	431	2.12	−4.44

η_1	η_2	η_3	η_4
0.260	0.476	0.478	0.483

For unpolarized TMD PDFs and FFs, we adopt the SV19 fit [43], in which the nonperturbative functions f_{NP} and D_{NP} are parametrized as

$$f_{\mathrm{NP}}(x,b_T) = \exp\left[-\frac{\lambda_1(1-x)+\lambda_2 x + x(1-x)\lambda_5}{\sqrt{1+\lambda_3 x^{\lambda_4} b_T^2}} b_T^2\right], \tag{54}$$

$$D_{\mathrm{NP}}(z,b_T) = \exp\left[-\frac{\eta_1 z + \eta_2(1-z)}{\sqrt{1+\eta_3(b_T/z)^2}} \frac{b_T^2}{z^2}\right]\left(1+\eta_4 \frac{b_T^2}{z^2}\right). \tag{55}$$

The values of the parameters λ_i and η_i are listed in Table II, which can be also found in [43,48]. For the FFs to charged hadrons, we approximate them as

$$D_{1,f\to h^+} = D_{1,f\to\pi^+} + D_{1,f\to K^+} + D_{1,f\to p}, \tag{56}$$

$$D_{1,f\to h^-} = D_{1,f\to\pi^-} + D_{1,f\to K^-} + D_{1,f\to\bar{p}}. \tag{57}$$

In this analysis, we include the SIDIS longitudinal-transverse double spin asymmetry data from HERMES [30], COMPASS [31–33], and JLab [34], as summarized in Table III. Since the TMD factorization is only valid at small $\delta = |P_{hT}|/(zQ)$, only data with $\delta < 0.5$ are included in the fit.

TABLE III. The SIDIS double spin asymmetry data by HERMES [30], COMPASS [31–33], and JLab [34]. The SFA refers to $\langle 2\cos(\phi_h - \phi_S)\sigma_{LT}\rangle/(\sqrt{1-\varepsilon^2}\langle\sigma_{UU}\rangle)$, and the CSA refers to $\langle 2\cos(\phi_h - \phi_S)\sigma_{LT}\rangle/\langle\sigma_{UU}\rangle$.

Dataset	Target	Beam	Original data points	Data points after cut $\delta < 0.5$, $Q > 1$ GeV	Data points after cut $\delta < 0.3$, $Q > 1$ GeV	Process	Measurement
HERMES [30]	H_2	27.6 GeV$e^{\pm}$	64	26	11	$e^{\pm}p \to e^{\pm}\pi^{+}X$	SFA
			64	26	11	$e^{\pm}p \to e^{\pm}\pi^{-}X$	SFA
			64	26	12	$e^{\pm}p \to e^{\pm}K^{+}X$	SFA
			64	26	12	$e^{\pm}p \to e^{\pm}K^{-}X$	SFA
			64	30	15	$e^{\pm}p \to e^{\pm}pX$	SFA
COMPASS [31]	NH_3	160 GeVμ^{+}	66	28	9	$\mu^{+}p \to \mu^{+}h^{+}X$	SFA
			66	26	8	$\mu^{+}p \to \mu^{+}h^{-}X$	SFA
JLab [34]	^{3}He	5.9 GeVe^{-}	4	2	1	$e^{-}n \to e^{-}\pi^{+}X$	CSA
			4	2	1	$e^{-}n \to e^{-}\pi^{-}X$	CSA
Total			460	192	80		

For the HERMES data, experimental results are provided in both one-dimensional binning and three-dimensional binning. We only use the three-dimensional bins in this study, because they are supposed to contain more information for the study of TMDs, which are multidimensional functions. For the COMPASS data, the experimental results are provided in one-dimensional binning but on x, z, and P_{hT} respectively. Since they tell the dependence on different variables, we include all these bins in the fit. However, to avoid double counting, we multiply a factor of $1/3$ when calculating the χ^2 from the COMPASS data. Then the total χ^2/N to be minimized in the fit is defined as

$$\chi^2/N = \frac{\frac{1}{3}\chi^2_{\mathrm{COMPASS}} + \chi^2_{\mathrm{HERMES}} + \chi^2_{\mathrm{JLab}}}{\frac{1}{3}N_{\mathrm{COMPASS}} + N_{\mathrm{HERMES}} + N_{\mathrm{JLab}}}, \qquad (58)$$

where $N_{\text{data set}}$ represents the number of points for each dataset. For each dataset, we have

$$\chi^2_{\text{data set}} = \sum_{\substack{i,j\in\\ \text{data-points}}} (t_i - a_i) V^{-1}_{ij} (t_j - a_j), \qquad (59)$$

where i and j run over all points in each set, t_i represent the theoretical values, and a_i represent experimental values. The V-matrix is given by

$$V_{ij} = \delta_{ij} (\sigma_i^{\mathrm{uncor}})^2 + \sigma_i^{\mathrm{cor}} \sigma_j^{\mathrm{cor}}, \qquad (60)$$

where $\sigma_i^{\mathrm{uncor}}$ and σ_i^{cor} stand for uncorrelated and correlated uncertainties, respectively.

As the existing world data are not precise enough to constrain all parameters introduced in Eq. (46), we practically reduce the number of parameters by imposing the conditions,

$$\alpha_u = \alpha_d = \alpha, \qquad \beta_u = \beta_d = \beta, \qquad r_u = r_d = r, \qquad (61)$$

and assume vanishing distributions for sea quarks, $\bar{u}$, $\bar{d}$, s, and $\bar{s}$. In the end, we have five free parameters to be determined as listed in Table IV.

To estimate the uncertainties, we create 1000 replicas of the data by smearing the central values of each data point according to a Gaussian distribution with data uncertainties being the widths. For each replica, we perform a fit. Then the central values of all physical quantities are evaluated from the average of the 1000 fits. More details of this approach are described in Ref. [48].

TABLE IV. Results of parameters for world data fit. The values and uncertainties are provided in two forms. The second column presents 68% CL indicated by upper and lower boundaries and the central values as the average of results within the ranges. The third column corresponds to the central values evaluated from the average of 1000 replicas and the uncertainties given by the standard deviations (STD) in two sides. The value of r is provided in unit of GeV^2 and all other parameters are dimensionless.

Parameter	Value within 68% CL	Average value with STD
N_u	$0.0206^{+0.0058}_{-0.0050}$	$0.0213^{+0.0100}_{-0.0056}$
N_d	$-0.0073^{+0.0079}_{-0.0082}$	$-0.0082^{+0.0092}_{-0.0175}$
α	$16.59^{+65.88}_{-10.11}$	$36.96^{+135.39}_{-27.30}$
β	$5.57^{+28.65}_{-3.87}$	$14.68^{+59.12}_{-11.30}$
r	$1.52^{+9.25}_{-1.49} \times 10^{-9}$	$0.0055^{+0.1621}_{-0.0055}$

TABLE V. The list of results of χ^2/N of world data fit for each world dataset.

Dataset	Data points	χ^2/N
HERMES π^+ [30]	26	1.01
HERMES π^- [30]	26	0.75
HERMES K^+ [30]	26	1.09
HERMES K^- [30]	26	0.68
HERMES P [30]	30	0.90
COMPASS h^+ [31]	28	0.44
COMPASS h^- [31]	26	0.65
JLab π^+ [34]	2	0.61
JLab π^- [34]	2	1.15
Total	192	0.84

In this study, we achieve total $\chi^2/N = 0.84$ as listed in Table V, together with χ^2 values for each dataset. The expectation values and uncertainties of the parameters are summarized in Table IV. In Figs. 2–6, we show the comparison between the fit results and experimental data, in which the filled points are included in the fit while the open points are not. The extracted worm-gear distribution functions $g_{1T}^{\perp}(x, k_T)$ are shown in Fig. 7 at several x-slices. As one can observe from the results, the u quark distribution is positive, while the d quark favors a negative distribution though still consistent with zero. This finding qualitatively agrees with the predictions from the quark model [11,17–20]. In addition, we also evaluate the transverse moments of the worm-gear distributions,

$$g_{1T}^{\perp(0)}(x) = 2\pi \int_0^{k_T^{\max}} k_T dk_T g_{1T}^{\perp}(x, k_T), \qquad (62)$$

$$g_{1T}^{\perp(1)}(x) = 2\pi \int_0^{k_T^{\max}} k_T dk_T \left(\frac{k_T^2}{2M^2}\right) g_{1T}^{\perp}(x, k_T), \qquad (63)$$

where the truncation is chosen as $k_T^{\max} = 1$ GeV. The results are shown in Figs. 8–12. The comparison between our results and those in Refs. [35] and [36] is shown in Fig. 8.

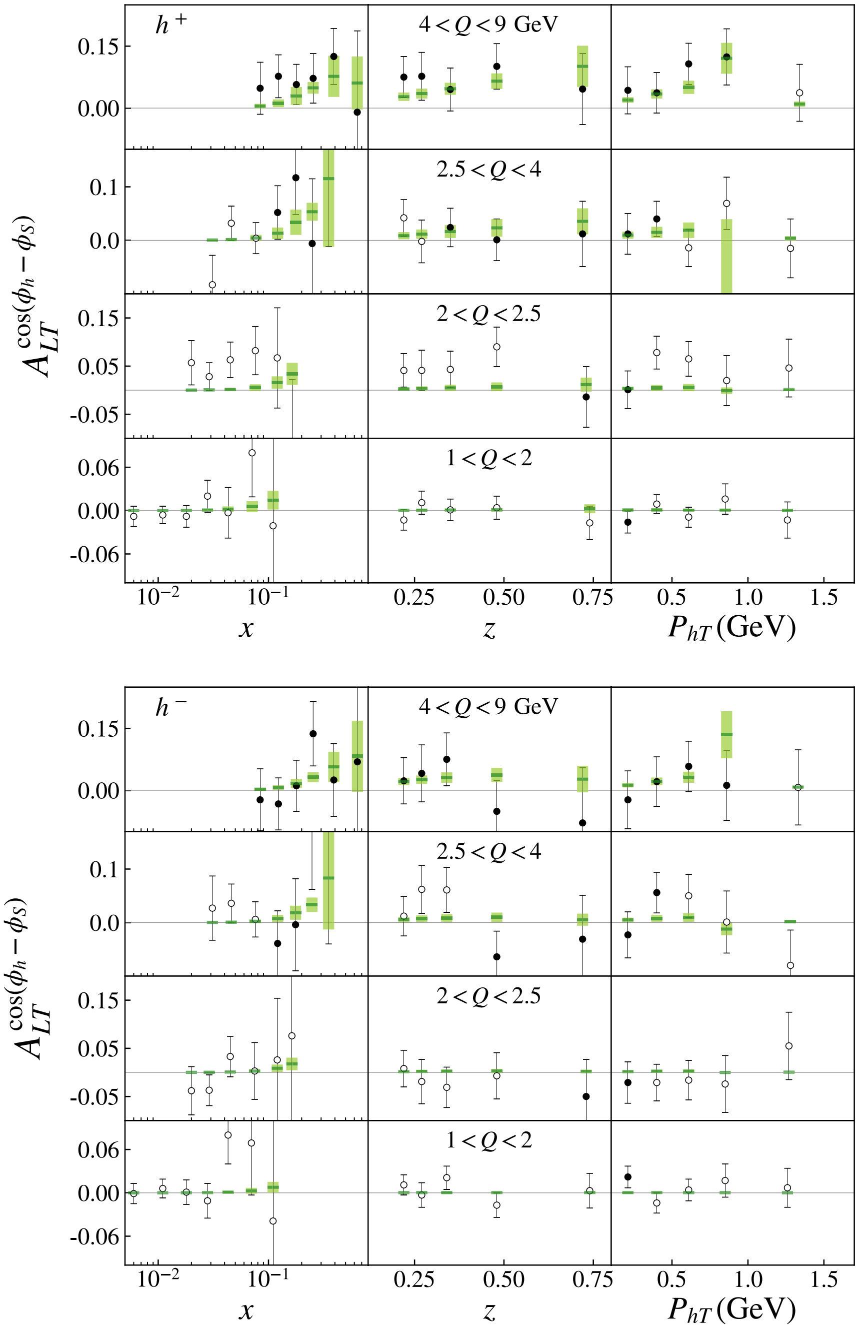

FIG. 2. Comparison between the fit results and the experimental data by COMPASS [31] from the proton target with charged hadron $h^{\pm}$ measured in the final state. The filled points are within the kinematic cuts, $\delta < 0.5$ and Q > 1 GeV, and included the fit, while the open points are not included in the fit. The green lines and the bands are the mean values and the standard deviations $(1-\sigma)$ calculated from the fits to 1000 replicas.

Our result are compatible with Ref. [36] but with larger uncertainties. This comes from the parametrization of the x dependence, which is fitted with free parameters in our analysis but is fixed in Ref. [36]. Compared with Ref. [35], the worm-gear distributions in our analysis are smaller. Such a difference arises from different choices of the unpolarized distributions f_1. We adopt the SV19 TMD parametrization of f_1, which after k_T integration is smaller than the collinear f_1 utilized in Ref. [35]. Since the analyses of $g_{1T}^{\perp}$ are based on asymmetry data, which correspond to the ratio $g_{1T}^{\perp}/f_1$, it is expected that our extracted $g_{1T}^{\perp}$ distributions are smaller.

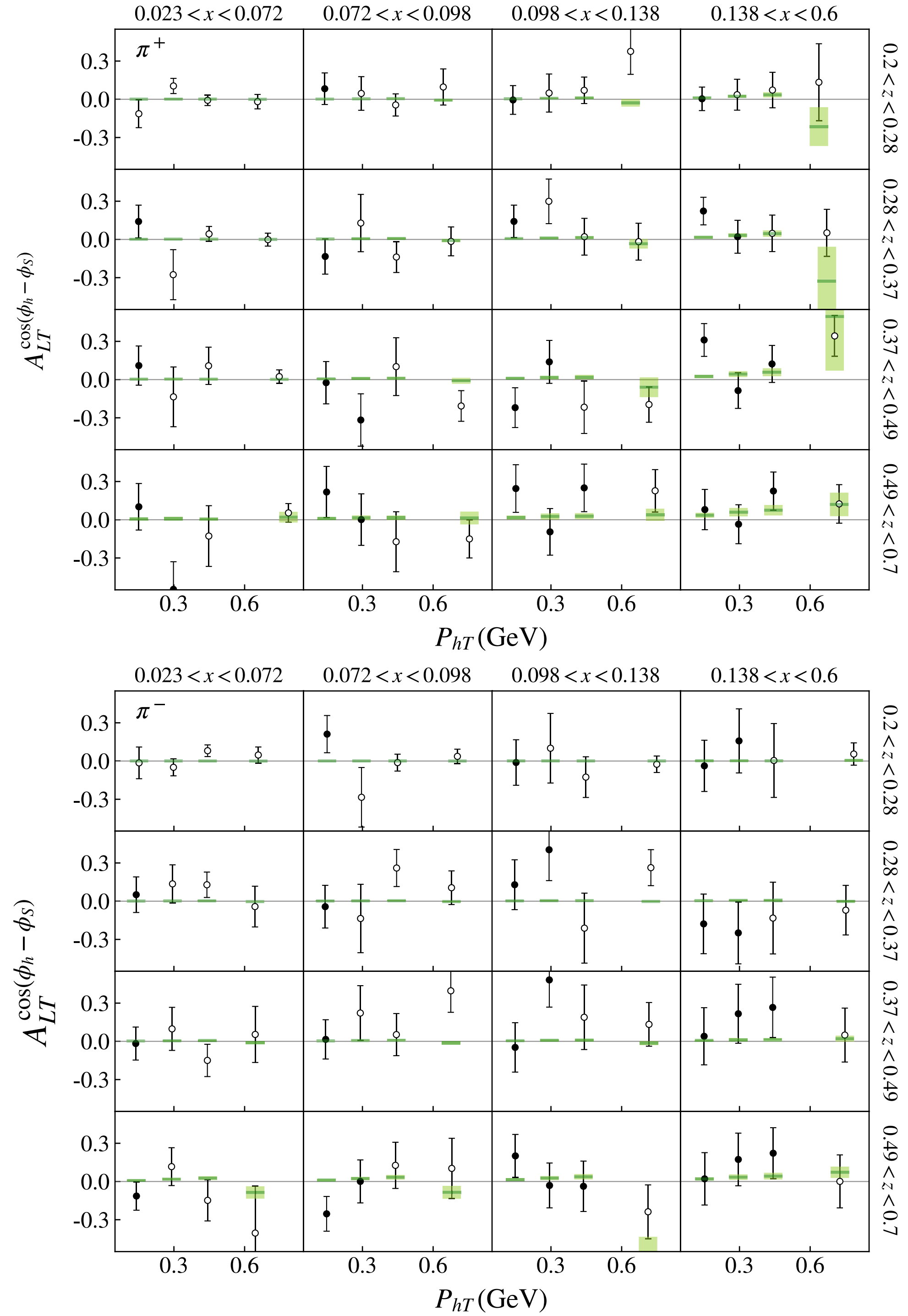

FIG. 3. Comparison between the fit results and the experimental data by HERMES [30] from the proton target with $\pi^{\pm}$ measured in the final state. The data points and the fit bands follow the same notations as Fig. 2.

We also test the effect of the weighting factor for COMPASS data in our analysis. The results of an unweighted fit are consistent with the weighted fit within error bands, while the unweighted fit shows slightly smaller peak value than the weighted fit.

Additionally, we also perform a world data fit including sea quarks, which as expected leads to larger uncertainties of *u* and *d* quarks. However, the sea quark distributions are largely unconstrained with error bands surrounding zero. Considering the purpose of this study is to estimate the

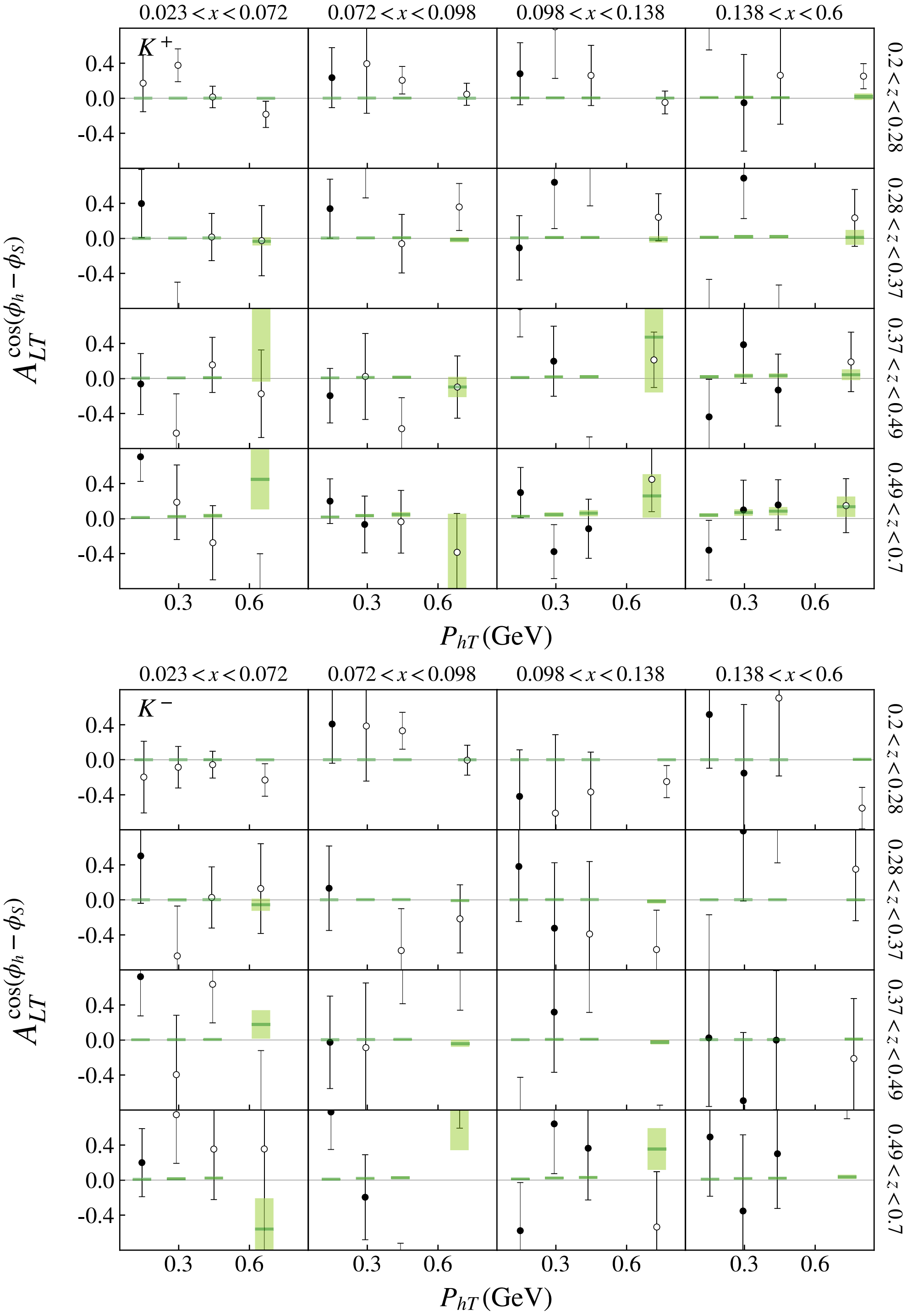

FIG. 4. Comparison between the fit results and experimental data by HERMES [30] from the proton target with $K^{\pm}$ measured in the final state. The data points and the fit bands follow the same notations as Fig. 2.

impact of the future EicC experiment, we generate the EicC pseudodata assuming vanishing worm-gear distributions of sea quarks.

IV. EICC PROJECTIONS

The EicC events are generated at the vertex level using the SIDIS Monte Carlo generator, which has been used in previous studies [48,49]. To select events in the DIS region, we apply the cuts,

$$Q^2 > 1\ \text{GeV}, \qquad 0.3 < z < 0.7, \tag{64}$$

$$W > 5\ \text{GeV}, \qquad W' > 2\ \text{GeV}, \tag{65}$$

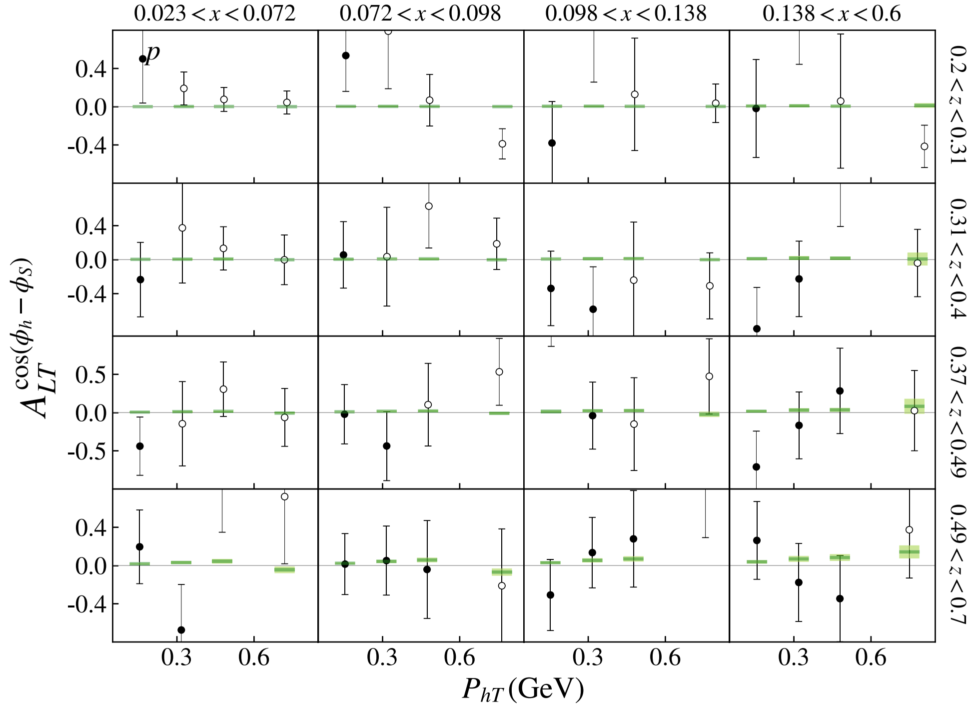

FIG. 5. Comparison between the fit results and the experimental data by HERMES [30] from the proton target with a fragmented proton measured in the final state. The data points and the fit bands follow the same notation as Fig. 2.

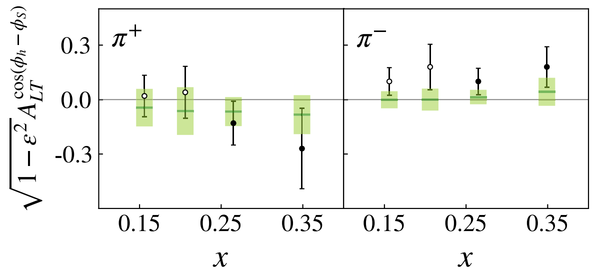

FIG. 6. Comparison between the fit results and the experimental data by JLab [34] from the effectively polarized neutron target with $\pi^{\pm}$ measured in the final state. The data points and the fit bands follow the same notation as Fig. 2.

where $W = \sqrt{(q+P)^2}$ is the invariant mass of the hadronic system, and $W' = \sqrt{(q+P-P_h)^2}$ is the missing mass. According to the detection conditions of the designed EicC detector, we further require the scattered electron momentum $P_e > 0.35$ GeV and the hadron momentum $P_h > 0.3$ GeV. In the simulation, we take the 3.5 GeV polarized electron beam with 80% polarization, the 20 GeV transversely polarized proton beam with 70% polarization, and the 40 GeV transversely polarized ^{3}He beam with 70% polarization. Aiming at a complete separation of contributions from all light flavor quarks, we take into account both $\pi^{\pm}$ and $K^{\pm}$ data.

To quantify the impact, we assume 50 fb^{-1} integrated luminosities of ep and e^3He collisions, which can be achieved with about one-year run according to the proposed instantaneous luminosity. For the systematic uncertainties, we assign 2% relative uncertainty to the polarization of the electron beam, 3% relative uncertainty to the polarization of the ion beam, and 5% relative uncertainty to the ^{3}He nuclear effect. These are expected the dominant sources of systematic uncertainties based on our current knowledge from existing polarized SIDIS measurements. Because the detailed design of the detectors are still unavailable, we leave more realistic estimation of systematic uncertainties to future studies.

The central values of the worm-gear asymmetry for the EicC pseudodata are evaluated from world data fit, which only include nonvanishing contributions from u and d quarks. Owing to the considerable amount of the expected EicC data, we can adopt stricter criteria to select data in the TMD region. Hence we set the cut as $\delta < 0.3$, and 5008 pseudodata points are included. Besides, we also free the parameters N_q for sea quark distributions and choose the same r_q for $\bar{u}$, $\bar{d}$, s, and $\bar{s}$ as

$$r_s = r_{\bar{u}} = r_{\bar{d}} = r_{\bar{s}} = (r_u + r_d)/2. \tag{66}$$

Then there are 12 free parameters in our fit summarized in Table VI. Following the same procedure, we perform a

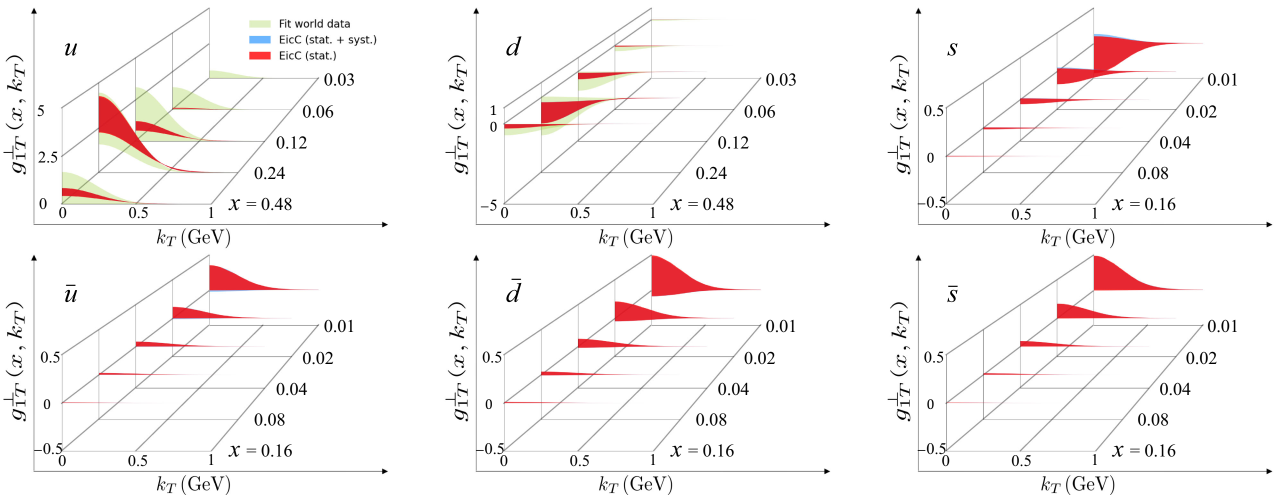

FIG. 7. The worm-gear distributions $g_{1T}^{\perp}(x, k_T)$ at the scale $Q = 2$ GeV. The uncertainty bands correspond to 68% CL estimated from the fits to 1000 replicas. The green bands are extracted distributions by fitting the world SIDIS data, the red bands are EicC projections with only statistical uncertainties, and the blue bands are EicC projections with both statistical and systematic uncertainties.

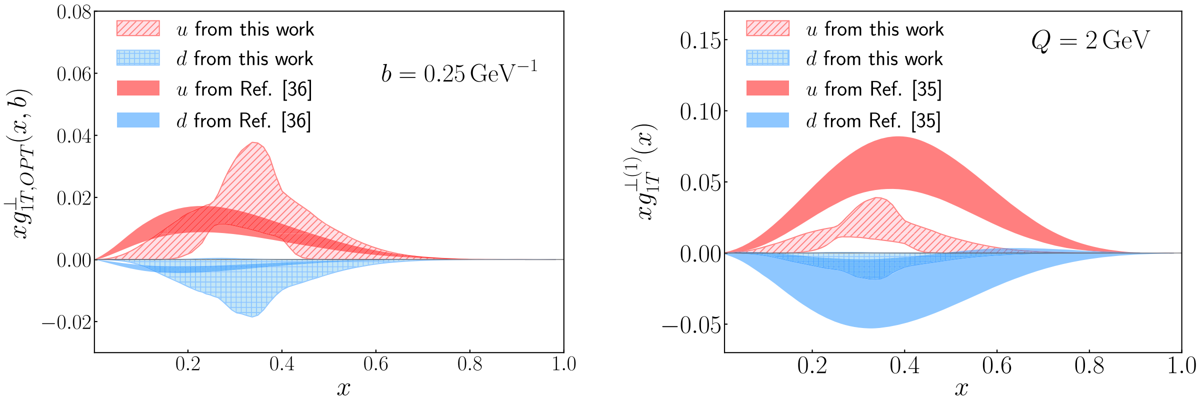

FIG. 8. The left (right) one show the results of optimal worm-gear functions (first transversal moment) of up quarks and down quarks. We also compare them with existing extractions. The bands of our results are correspond to 68% confidence level (CL) while bands of comparison counterparts are taken from Refs. [35,36].

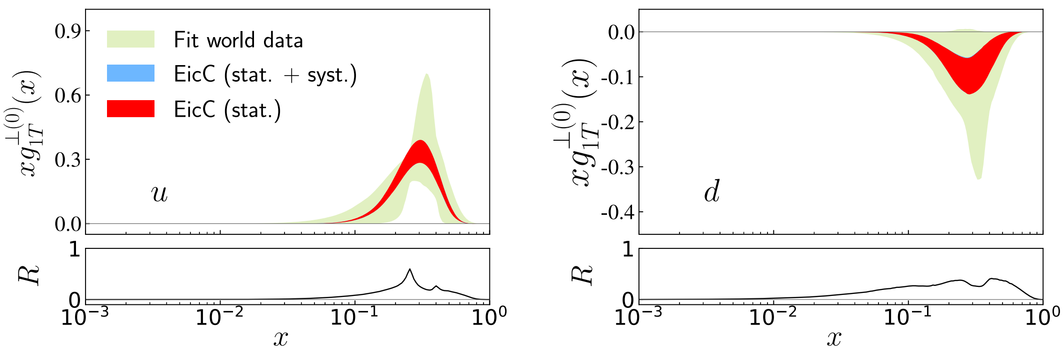

FIG. 9. The zeroth transverse moment of the worm-gear functions, $g_{1T}^{\perp(0)}(x)$ as defined in Eq. (62), for u and d quarks at the scale $Q = 2$ GeV. The uncertainty bands correspond to 68% CL estimated from the fits to 1000 replicas. The green bands are extracted distributions by fitting the world SIDIS data, the red bands are EicC projections with only statistical uncertainties, and the blue bands are EicC projections with both statistical and systematic uncertainties. R is the ratio of uncertainty of the result of pseudodata data fit to that of world fit.

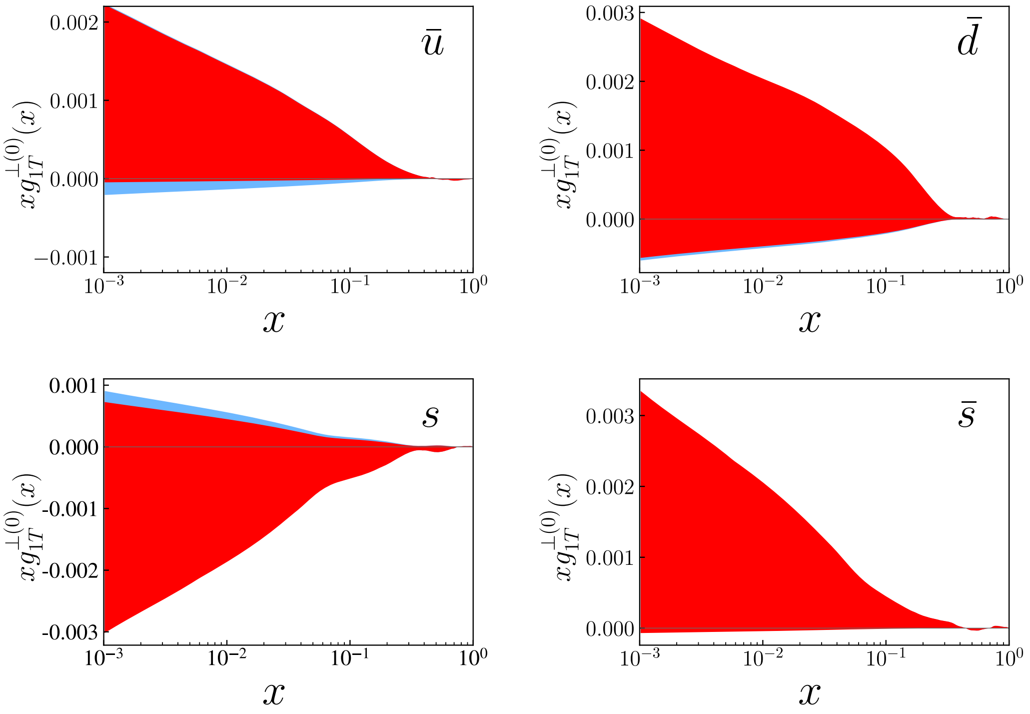

FIG. 10. EicC projections of the zeroth transverse moment of the worm-gear functions, $g_{1T}^{\perp(0)}(x)$ as defined in Eq. (62), for $\bar{u}$, $\bar{d}$, s, and $\bar{s}$ quarks at the scale $\mathrm{Q} = 2$ GeV. The uncertainty bands correspond to 68% CL estimated from the fits to 1000 replicas. The red bands only contain statistical uncertainties, and the blue bands contain both statistical and systematic uncertainties.

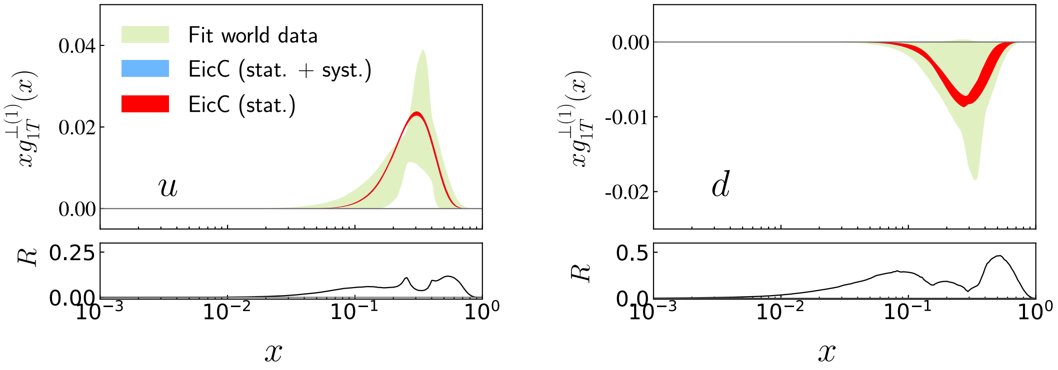

FIG. 11. The first transverse moment of the worm-gear functions, $g_{1T}^{\perp(1)}(x)$ as defined in Eq. (63), for u and d quarks at the scale $\mathrm{Q} = 2$ GeV. The uncertainty bands correspond to 68% CL estimated from the fits to 1000 replicas. The green bands are extracted distributions by fitting the world SIDIS data, the red bands are EicC projections with only statistical uncertainties, and the blue bands are EicC projections with both statistical and systematic uncertainties. R is the ratio of uncertainty of the result of pseudodata data fit to that of world fit.

simultaneous fit to the world data and the EicC pseudodata. This analysis gives $\chi^2/N = 1.09$ with corresponding values and uncertainties of the parameters listed in Table IV, which are evaluated from the fits to 1000 replicas. The EicC projections of the worm-gear distributions $g_{1T}^{\perp}(x, k_T)$ are shown in Fig. 7. The zeroth transverse momentum moments $g_{1T}^{\perp(0)}(x)$ are shown in Figs. 9 and 10, and the first transverse momentum moments $g_{1T}^{\perp(1)}(x)$ are shown in Figs. 11 and 12. Our results provide a proof of principle that it becomes possible to extract information on worm-gear functions of the sea quarks once has more data.

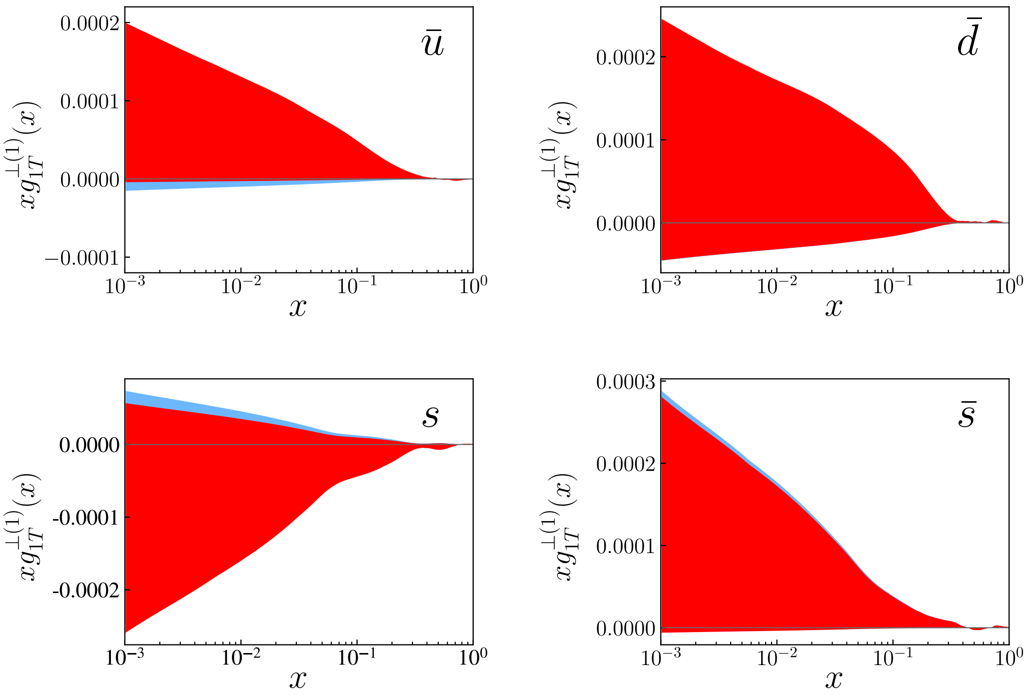

FIG. 12. EicC projections of the first transverse moment of the worm-gear functions, $g_{1T}^{\perp(1)}(x)$ as defined in Eq. (63), for $\bar{u}$, $\bar{d}$, s, and $\bar{s}$ quarks at the scale Q = 2 GeV. The uncertainty bands correspond to 68% CL estimated from the fits to 1000 replicas. The red bands only contain statistical uncertainties, and the blue bands contain both statistical and systematic uncertainties.

V. SUMMARY

In this work, we perform a global fit to the worm-gear asymmetries from SIDIS in small transverse momentum region, including the TMD evolution effect at the next-to-next-to-leading-logarithmic (NNLL) accuracy. Due to the fact that the existing experimental uncertainties are too large to determine the worm-gear distributions of sea quarks, only up and down quarks are considered in the global fit. Then an impact study is performed by including the EicC pseudodata in our global fit. For EicC pseudodata, the statistical uncertainties and dominant systematic uncertainties are taken into account. The latter is mainly due to the uncertainties from beam polarimetry and the uncertainties of ^{3}He nuclear effects.

Once the precise data are available from EicC, the precision of the worm-gear distributions for up and down quarks will be significantly improved. Meanwhile, it will also provide the opportunity to extract the worm-gear distributions of sea quarks. With much more expected precise data from EicC, one can extract the TMDs utilizing more flexible parametrizations and thus less biased determination of the nucleon spin structures. Owing to the high precision and a wide phase space coverage of EicC pseudodata, a more strict cut of δ, W, and W' will be feasible. It allows us to have cleaner selection of data required by the TMD factorization. On the other hand, the events in the transition region are also valuable to test the matching between TMD and collinear regions [50–57]. The combination of polarized ep and e^3He data at similar

TABLE VI. Results of parameters for EicC pseudodata fit. The central values are the average of the results from 1000 replicas, and the uncertainties correspond to 68% CL. The values of r_u and r_d are provided in unit of GeV^2 and the others are dimensionless. Results with only statistical (Stat.) uncertainties are listed in the second and fifth columns, and those with both statistical and systematic (Stat. + Syst.) uncertainties are listed in the third and sixth columns.

Parameter	Stat.	Stat. + Syst.	Parameter	Stat.	Stat. + Syst.
N_u	$0.0209^{+0.0006}_{-0.0006}$	$0.0209^{+0.0006}_{-0.0006}$	α_u	$12.46^{+0.72}_{-0.67}$	$12.47^{+0.67}_{-0.64}$
N_d	$-0.0077^{+0.0008}_{-0.0009}$	$-0.0077^{+0.0008}_{-0.0008}$	α_d	$13.01^{+4.68}_{-2.70}$	$12.94^{+6.22}_{-2.83}$
N_s	$-0.00023^{+0.00044}_{-0.00046}$	$-0.00026^{+0.00042}_{-0.00047}$	β_u	$4.46^{+0.26}_{-0.25}$	$4.46^{+0.23}_{-0.23}$
$N_{\bar{u}}$	$0.00019^{+0.00023}_{-0.00022}$	$0.00020^{+0.00024}_{-0.00021}$	β_d	$4.31^{+1.47}_{-0.88}$	$4.29^{+1.80}_{-0.90}$
$N_{\bar{d}}$	$0.00021^{+0.00032}_{-0.00031}$	$0.00022^{+0.00034}_{-0.00032}$	r_u	$0.0067^{+0.0050}_{-0.0048}$	$0.0067^{+0.0053}_{-0.0050}$
$N_{\bar{s}}$	$0.00038^{+0.00045}_{-0.00037}$	$0.00038^{+0.00045}_{-0.00037}$	r_d	$0.016^{+0.025}_{-0.016}$	$0.016^{+0.024}_{-0.016}$

kinematics are essential for a complete flavor separation. It is important to remark that the kinematic coverage of EicC will fill the gap between the on-going JLab-12 GeV program and the approved Electron-Ion Collider to be built at BNL. With all these facilities, we will be able to have a complete physical picture of nucleon three-dimensional structures, towards a profound understanding of strong interactions.

ACKNOWLEDGMENTS

This work is supported in part by the Strategic Priority Research Program of the Chinese Academy of Sciences under Grant No. XDB34000000, the Guangdong Major Project of Basic and Applied Basic Research No. 2020B0301030008, the Guangdong Provincial Key Laboratory of Nuclear Science with No. 2019B121203010, the National Natural Science Foundation of China under Grants No. 12175117 and No. 12321005, and Shandong Province Natural Science Foundation Grant No. ZFJH202303. P. S. is supported by the Natural Science Foundation of China under Grants No. 11975127 and No. 12061131006. B.-Q. M. is supported by National Natural Science Foundation of China under Grants No. 12075003 and No. 12335006. The authors also acknowledge the computing resource available at the Southern Nuclear Science Computing Center.

APPENDIX A: FOURIER TRANSFORMS FOR TMDS

The Fourier transforms for TMDs are

$$\begin{aligned} f_1(x,k_T) &= \int \frac{d^2\mathbf{b}_T}{4\pi^2} e^{i\mathbf{b}_T\cdot\mathbf{k}_T} f_1(x,b_T) \\ &= \int_0^{+\infty} \frac{b_T db_T}{2\pi} J_0(b_T k_T) f_1(x,b_T), \end{aligned} \tag{A1}$$

$$\begin{aligned} f_1(x,b_T) &= \int d^2\mathbf{k}_T e^{-i\mathbf{b}_T\cdot\mathbf{k}_T} f_1(x,k_T) \\ &= 2\pi \int_0^{+\infty} k_T dk_T J_0(b_T k_T) f_1(x,k_T), \end{aligned} \tag{A2}$$

$$\begin{aligned} \frac{k_T}{M} g_{1T}^{\perp}(x,k_T) &= \int \frac{d^2\mathbf{b}_T}{4\pi^2} e^{i\mathbf{b}_T\cdot\mathbf{k}_T} (-ib_T M) g_{1T}^{\perp}(x,b_T), \\ g_{1T}^{\perp}(x,k_T) &= \frac{M^2}{k_T} \int_0^{+\infty} \frac{b_T^2 db_T}{2\pi} J_1(b_T k_T) g_{1T}^{\perp}(x,b_T), \end{aligned} \tag{A3}$$

$$\begin{aligned} (-iMb_T) g_{1T}^{\perp}(x,b_T) &= \int d^2\mathbf{k}_T e^{-i\mathbf{b}_T\cdot\mathbf{k}_T} \frac{k_T}{M} g_{1T}^{\perp}(x,k_T), \\ g_{1T}^{\perp}(x,b_T) &= \frac{2\pi}{M^2 b_T} \int_0^{+\infty} k_T^2 dk_T J_1(b_T k_T) \\ &\quad \times g_{1T}^{\perp}(x,k_T), \end{aligned} \tag{A4}$$

$$\begin{aligned} D_1(z,k_T) &= \int \frac{d^2\mathbf{b}_T}{4\pi^2} e^{-i\mathbf{b}_T\cdot\mathbf{k}_T} D_1(z,b_T) \\ &= \int_0^{+\infty} \frac{b_T db_T}{2\pi} J_0(b_T k_T) D_1(z,b_T), \end{aligned} \tag{A5}$$

$$\begin{aligned} D_1(z,b_T) &= \int d^2\mathbf{k}_T e^{i\mathbf{b}_T\cdot\mathbf{k}_T} D_1(z,k_T) \\ &= 2\pi \int_0^{+\infty} k_T dk_T J_0(b_T k_T) D_1(z,k_T). \end{aligned} \tag{A6}$$

APPENDIX B: EXPRESSIONS FOR ENERGY EVOLUTION FACTOR

The $\mathcal{D}(Q,b_T)$ is the rapidity anomalous dimension (RAD). At large values of b_T, the $\mathcal{D}(Q,b_T)$ behaves like a linear function of b_T, which is suggested by some models such as [58,59]. Therefore, we parametrize the RAD as

$$\mathcal{D}(\mu,b_T) = \mathcal{D}_{\mathrm{resum}}(\mu, b_T^*(b_T)) + c_0 b_T b_T^*(b_T), \tag{B1}$$

where the $\mathcal{D}_{\mathrm{resum}}(\mu, b_T^*(b_T))$ is the resummed perturbative expansion of RAD, and $b_T^*(b_T)$ take the form

$$b_T^*(b_T) = \frac{b_T}{\sqrt{1 + b_T^2/B_{\mathrm{NP}}^2}}. \tag{B2}$$

At small values of b_T, the term $c_0 b_T b_T^*(b_T)$ can be ignored and the term $\mathcal{D}_{\mathrm{resum}}$ is dominant, while at large values of b_T, the $\mathcal{D}$ behave like $c_0 B_{\mathrm{NP}} b_T$. We take $B_{\mathrm{NP}} = 1.93\ \mathrm{GeV}^{-1}$ and $c_0 = 0.0391\ \mathrm{GeV}^2$ as determined in SV19 model [43]. The $\mathcal{D}_{\mathrm{resum}}$ can be represented as

$$\begin{aligned} \mathcal{D}_{\mathrm{resum}}(\mu,b_T) = &-\frac{\Gamma_0}{2\beta_0}\ln(1-X) + \frac{a_s}{2\beta_0(1-X)}\left[-\frac{\beta_1\Gamma_0}{\beta_0}(\ln(1-X)+X) + \Gamma_1 X\right] + \frac{a_s^2}{(1-X)^2}\left[\frac{\Gamma_0\beta_1^2}{4\beta_0^3}(\ln^2(1-X) - X^2)\right. \\ &\left. + \frac{\beta_1\Gamma_1}{4\beta_0^2}(X^2 - 2X - 2\ln(1-X)) + \frac{\Gamma_0\beta_2}{4\beta_0^2}X^2 - \frac{\Gamma_2}{4\beta_0}X(X-2) + C_F C_A\left(\frac{404}{27} - 14\zeta_3\right) - \frac{112}{27}T_R N_f C_F\right], \end{aligned} \tag{B3}$$

where $X = \beta_0 a_s \mathbf{L}_\mu$, β_i are coefficients of anomaly dimension of strong coupling constant, which satisfies

$$\mu^2 \frac{d a_s(\mu)}{d\mu^2} = -\beta(a_s) = -\sum_{i=0}^{\infty} a_s^{i+2}(\mu)\beta_i. \tag{B4}$$

$C_A = 3$ and $T_R = 1/2$ are color factors of the $SU(3)$. The Γ_i are coefficients of expansion of CUSP anomaly dimension $\Gamma_{\text{cusp}}(\mu)$, which is related with the integrability condition (24) of the evolution equation. The Γ_i are defined by

$$\Gamma_{\text{cusp}}(\mu) = \sum_{i=0}^{\infty} a_s^{i+1}\Gamma_i. \tag{B5}$$

With the CUSP anomaly dimension, the anomaly dimension γ_V can be written as

$$\gamma_F(\mu, \zeta) = \Gamma_{\text{cusp}}(\mu) \ln\left(\frac{\mu^2}{\zeta}\right) - \gamma_V(\mu), \tag{B6}$$

and the $\gamma_V(\mu)$ can be expanded as

$$\gamma_V(\mu) = \sum_{i=1}^{\infty} a_s^n \gamma_i. \tag{B7}$$

The Γ_i and γ_i can be determined perturbatively, and up to two-loop level,

$$\begin{aligned}
\Gamma_0 &= 4C_F, \\
\Gamma_1 &= 4C_F\left[\left(\frac{67}{9} - \frac{\pi^2}{3}\right)C_A - \frac{20}{9}T_R N_f\right], \\
\gamma_1 &= -6C_F, \\
\gamma_2 &= C_F^2(-3 + 4\pi^2 - 48\zeta_3) \\
&\quad + C_F C_A\left(-\frac{961}{27} - \frac{11\pi^2}{3} + 52\zeta_3\right) \\
&\quad + C_F T_R N_f\left(\frac{260}{27} + \frac{4\pi^2}{3}\right),
\end{aligned} \tag{B8}$$

TABLE VII. Values of N_f at different values of energy scale.

$\mu \leq 1.27$ GeV	$N_f = 3$
$1.27 < \mu \leq 4.18$ GeV	$N_f = 4$
$\mu > 4.18$ GeV	$N_f = 5$

where N_f is the number of active quark flavors and have different values at different energy scales (see Table VII), $\zeta_3 \approx 1.202$ is the Apéry's constant.

Due to that the nonperturbative corrections to the RAD can not be ignored at large-b_T, we need to use the exact solution of ζ_μ at large-b_T; while at very small-b_T, we use the perturbative solution. In order to connect these two region, we introduce a $e^{-b_T^2/B_{\text{NP}}^2}$ factor, and the ζ_μ is expressed as [43]

$$\zeta_\mu(b_T) = \zeta_\mu^{\text{pert}}(b_T) e^{-\frac{b_T^2}{B_{\text{NP}}^2}} + \zeta_\mu^{\text{exact}}(b_T)\left(1 - e^{-\frac{b_T^2}{B_{\text{NP}}^2}}\right). \tag{B9}$$

Therefore, at $b_T^2 \ll B_{\text{NP}}^2$, ζ_μ is dominantly given by perturbative solution, and at other regions, it will turn to exact solution. We express the ζ_μ^{pert} and ζ_μ^{exact} here,

$$\zeta_\mu^{\text{pert}}(\mu, b_T) = \frac{2\mu e^{-\gamma_E}}{b_T} e^{-v(\mu, b_T)}, \tag{B10}$$

$$\zeta_\mu^{\text{exact}}(\mu, b_T) = \mu^2 e^{-g(\mu, b_T)/\mathcal{D}(\mu, b_T)}, \tag{B11}$$

where

$$v(\mu, b_T) = \frac{\gamma_1}{\Gamma_0} + a_s\left[\frac{\beta_0}{12}\mathbf{L}_\mu^2 + \frac{\gamma_2 + d_2(0)}{\Gamma_0} - \frac{\gamma_1 \Gamma_1}{\Gamma_0^2}\right], \tag{B12}$$

and

$$\begin{aligned}
g(\mu, b_T) = \frac{1}{a_s}\frac{\Gamma_0}{2\beta_0^2}\Bigg\{& e^{-p} - 1 + p + a_s\left[\frac{\beta_1}{\beta_0}\left(e^{-p} - 1 + p - \frac{p^2}{2}\right) - \frac{\Gamma_1}{\Gamma_0}(e^{-p} - 1 + p) + \frac{\beta_0\gamma_1}{\Gamma_0}p\right] \\
&+ a_s^2\left[\left(\frac{\Gamma_1^2}{\Gamma_0^2} - \frac{\Gamma_2}{\Gamma_0}\right)(\cosh p - 1) + \left(\frac{\beta_1\Gamma_1}{\beta_0\Gamma_0} - \frac{\beta_2}{\beta_0}\right)(\sinh p - p) + \left(\frac{\beta_0\gamma_2}{\Gamma_0} - \frac{\beta_0\gamma_1\Gamma_1}{\Gamma_0^2}\right)(e^p - 1)\right]\Bigg\}.
\end{aligned} \tag{B13}$$

In the $g(\mu, b_T)$, the p is

$$p = \frac{2\beta_0 \mathcal{D}(\mu, b_T)}{\Gamma_0}, \tag{B14}$$

and in the $v(\mu, b_T)$, the $d_2(0)$ is

$$d_2(0) = C_F C_A\left(\frac{404}{27} - 14\zeta_3\right) - \frac{112}{27}T_R N_f C_F. \tag{B15}$$

[1] R. D. Tangerman and P. J. Mulders, Intrinsic transverse momentum and the polarized Drell-Yan process, Phys. Rev. D **51**, 3357 (1995).

[2] P. J. Mulders and R. D. Tangerman, The complete tree level result up to order 1/Q for polarized deep inelastic leptoproduction, Nucl. Phys. **B461**, 197 (1996); **B484**, 538 (1997).

[3] D. Boer and P. J. Mulders, Time reversal odd distribution functions in leptoproduction, Phys. Rev. D **57**, 5780 (1998).

[4] X. d. Ji and F. Yuan, Parton distributions in light cone gauge: Where are the final state interactions?, Phys. Lett. B **543**, 66 (2002).

[5] J. Zhu and B. Q. Ma, Three-dimensional parton distribution functions g_{1T} and $h_{1L}^{\perp}$ in the polarized proton-antiproton Drell-Yan process, Eur. Phys. J. C **71**, 1807 (2011).

[6] J. Zhu and B. Q. Ma, Proposal for measuring new transverse momentum dependent parton distributions g_{1T} and $h_{1L}^{\perp}$ through semi-inclusive deep inelastic scattering, Phys. Lett. B **696**, 246 (2011).

[7] Xuan Luo and H. Sun, Kotzinian-Mulders effect in semi-inclusive DIS within TMD factorization, Chin. Phys. C **46**, 023102 (2022).

[8] A. M. Kotzinian and P. J. Mulders, Longitudinal quark polarization in transversely polarized nucleons, Phys. Rev. D **54**, 1229 (1996).

[9] G. A. Miller, Densities, parton distributions, and measuring the non-spherical shape of the nucleon, Phys. Rev. C **76**, 065209 (2007).

[10] A. Bacchetta, F. Conti, and M. Radici, Transverse-momentum distributions in a diquark spectator model, Phys. Rev. D **78**, 074010 (2008).

[11] B. Pasquini, S. Cazzaniga, and S. Boffi, Transverse momentum dependent parton distributions in a light-cone quark model, Phys. Rev. D **78**, 034025 (2008).

[12] B. Pasquini, S. Boffi, and P. Schweitzer, The spin structure of the nucleon in light-cone quark models, Mod. Phys. Lett. A **24**, 2903 (2009).

[13] M. Burkardt, Spin-orbit correlations and single-spin asymmetries, in *Exclusive Reactions at High Momentum Transfer* (World Scientific, Singapore, 2008).

[14] R. Jakob, P. J. Mulders, and J. Rodrigues, Modeling quark distribution and fragmentation functions, Nucl. Phys. **A626**, 937 (1997).

[15] A. V. Efremov, P. Schweitzer, O. V. Teryaev, and P. Zavada, Transverse momentum dependent distribution functions in a covariant parton model approach with quark orbital motion, Phys. Rev. D **80**, 014021 (2009).

[16] H. Avakian, A. V. Efremov, P. Schweitzer, and F. Yuan, The transverse momentum dependent distribution functions in the bag model, Phys. Rev. D **81**, 074035 (2010).

[17] A. Bacchetta, M. Boglione, A. Henneman, and P. J. Mulders, Bounds on transverse momentum dependent distribution and fragmentation functions, Phys. Rev. Lett. **85**, 712 (2000).

[18] X. d. Ji, J. P. Ma, and F. Yuan, Three quark light cone amplitudes of the proton and quark orbital motion dependent observables, Nucl. Phys. **B652**, 383 (2003).

[19] S. Boffi, A. V. Efremov, B. Pasquini, and P. Schweitzer, Azimuthal spin asymmetries in light-cone constituent quark models, Phys. Rev. D **79**, 094012 (2009).

[20] A. Bacchetta, M. Radici, F. Conti, and M. Guagnelli, Weighted azimuthal asymmetries in a diquark spectator model, Eur. Phys. J. A **45**, 373 (2010).

[21] L. P. Gamberg, G. R. Goldstein, and M. Schlegel, Transverse quark spin effects and the flavor dependence of the Boer-Mulders function, Phys. Rev. D **77**, 094016 (2008).

[22] P. V. Pobylitsa, Transverse momentum dependent parton distributions in large N_c QCD, arXiv:hep-ph/0301236.

[23] H. Avakian, A. V. Efremov, K. Goeke, A. Metz, P. Schweitzer, and T. Teckentrup, Are there approximate relations among transverse momentum dependent distribution functions?, Phys. Rev. D **77**, 014023 (2008).

[24] A. Accardi, A. Bacchetta, W. Melnitchouk, and M. Schlegel, What can break the Wandzura-Wilczek relation?, J. High Energy Phys. 11 (2009) 093.

[25] K. Kanazawa, Y. Koike, A. Metz, D. Pitonyak, and M. Schlegel, Operator constraints for twist-3 functions and Lorentz invariance properties of twist-3 observables, Phys. Rev. D **93**, 054024 (2016).

[26] I. Scimemi and A. Vladimirov, Matching of transverse momentum dependent distributions at twist-3, Eur. Phys. J. C **78**, 802 (2018).

[27] P. Hagler, B. U. Musch, J. W. Negele, and A. Schafer, Intrinsic quark transverse momentum in the nucleon from lattice QCD, Europhys. Lett. **88**, 61001 (2009).

[28] B. U. Musch, P. Hagler, J. W. Negele, and A. Schafer, Exploring quark transverse momentum distributions with lattice QCD, Phys. Rev. D **83**, 094507 (2011).

[29] B. Yoon, M. Engelhardt, R. Gupta, T. Bhattacharya, J. R. Green, B. U. Musch, J. W. Negele, A. V. Pochinsky, A. Schäfer, and S. N. Syritsyn, Nucleon transverse momentum-dependent parton distributions in lattice QCD: Renormalization patterns and discretization effects, Phys. Rev. D **96**, 094508 (2017).

[30] A. Airapetian *et al.* (HERMES Collaboration), Azimuthal single- and double-spin asymmetries in semi-inclusive deep-inelastic lepton scattering by transversely polarized protons, J. High Energy Phys. 12 (2020) 010.

[31] C. Adolph *et al.* (COMPASS Collaboration), Sivers asymmetry extracted in SIDIS at the hard scales of the Drell–Yan process at COMPASS, Phys. Lett. B **770**, 138 (2017).

[32] B. Parsamyan, Measurement of target-polarization dependent azimuthal asymmetries in SIDIS and Drell-Yan processes at COMPASS experiment, Proc. Sci. QCDEV2017 (**2018**) 042.

[33] H. Avakian, B. Parsamyan, and A. Prokudin, Spin orbit correlations and the structure of the nucleon, Riv. Nuovo Cimento **42**, 1 (2019).

[34] J. Huang *et al.* (Jefferson Lab Hall A Collaboration), Beam-target double spin asymmetry A_{LT} in charged pion production from deep inelastic scattering on a transversely polarized ^{3}He Target at $1.4 < \mathrm{Q}^2 < 2.7\ \mathrm{GeV}^2$, Phys. Rev. Lett. **108**, 052001 (2012).

[35] S. Bhattacharya, Z. B. Kang, A. Metz, G. Penn, and D. Pitonyak, First global QCD analysis of the TMD g1T from semi-inclusive DIS data, Phys. Rev. D **105**, 034007 (2022).

[36] M. Horstmann, A. Schafer, and A. Vladimirov, Study of the worm-gear-T function g1T with semi-inclusive DIS data, Phys. Rev. D **107**, 034016 (2023).

[37] A. Accardi, J. L. Albacete, M. Anselmino, N. Armesto, E. C. Aschenauer, A. Bacchetta, D. Boer, W. K. Brooks, T. Burton, N. B. Chang *et al.*, Electron Ion Collider: The next QCD frontier: Understanding the glue that binds us all, Eur. Phys. J. A **52**, 268 (2016).

[38] R. Abdul Khalek, A. Accardi, J. Adam, D. Adamiak, W. Akers, M. Albaladejo, A. Al-bataineh, M. G. Alexeev, F. Ameli, P. Antonioli *et al.*, Science requirements and detector concepts for the electron-ion collider: EIC yellow report, Nucl. Phys. **A1026**, 122447 (2022).

[39] D. P. Anderle, T. J. Hou, H. Xing, M. Yan, C. P. Yuan, and Y. Zhao, Determining the helicity structure of the nucleon at the Electron Ion Collider in China, J. High Energy Phys. 08 (2021) 034.

[40] A. Bacchetta, M. Diehl, K. Goeke, A. Metz, P. J. Mulders, and M. Schlegel, Semi-inclusive deep inelastic scattering at small transverse momentum, J. High Energy Phys. 02 (2007) 093.

[41] A. Bacchetta, U. D'Alesio, M. Diehl, and C. A. Miller, Single-spin asymmetries: The Trento conventions, Phys. Rev. D **70**, 117504 (2004).

[42] J. C. Collins and D. E. Soper, Back-to-back jets: Fourier transform from B to K-transverse, Nucl. Phys. **B197**, 446 (1982).

[43] I. Scimemi and A. Vladimirov, Non-perturbative structure of semi-inclusive deep-inelastic and Drell-Yan scattering at small transverse momentum, J. High Energy Phys. 06 (2020) 137.

[44] R. D. Ball *et al.* (NNPDF Collaboration), Parton distributions from high-precision collider data, Eur. Phys. J. C **77**, 663 (2017).

[45] D. de Florian, R. Sassot, M. Epele, R. J. Hernández-Pinto, and M. Stratmann, Parton-to-pion fragmentation reloaded, Phys. Rev. D **91**, 014035 (2015).

[46] D. de Florian, M. Epele, R. J. Hernández-Pinto, R. Sassot, and M. Stratmann, Parton-to-kaon fragmentation revisited, Phys. Rev. D **95**, 094019 (2017).

[47] D. de Florian, R. Sassot, and M. Stratmann, Global analysis of fragmentation functions for protons and charged hadrons, Phys. Rev. D **76**, 074033 (2007).

[48] C. Zeng, T. Liu, P. Sun, and Y. Zhao, Toward three-dimensional nucleon structures at the Electron-Ion Collider in China: A study of the Sivers function, Phys. Rev. D **106**, 094039 (2022).

[49] C. Zeng, H. Dong, T. Liu, P. Sun, and Y. Zhao, Role of sea quarks in the nucleon transverse spin, Phys. Rev. D **109**, 056002 (2024).

[50] J. Collins, Davison E. Soper, and G. Sterman, Transverse momentum distribution in Drell-Yan Pair and W and Z boson production, Nucl. Phys. **B250**, 199 (1985).

[51] J. Collins, *Foundations of Perturbative QCD*, Cambridge Monographs on Particle Physics, Nuclear Physics and Cosmology Series Vol. 32 (Cambridge University Press, Cambridge, England, 2011).

[52] J. Collins and T. C. Rogers, Equality of two definitions for transverse momentum dependent parton distribution functions, Phys. Rev. D **87**, 034018 (2013).

[53] P. Sun and F. Yuan, Transverse momentum dependent evolution: Matching semi-inclusive deep inelastic scattering processes to Drell-Yan and W/Z boson production, Phys. Rev. D **88**, 114012 (2013).

[54] M. Boglione, J. O. Gonzalez Hernandez, S. Melis, and A. Prokudin, A study on the interplay between perturbative QCD and CSS/TMD formalism in SIDIS processes, J. High Energy Phys. 02 (2015) 095.

[55] J. Collins and T. C. Rogers, Relating transverse momentum dependent and collinear factorization theorems in a generalized formalism, Phys. Rev. D **94**, 034014 (2016).

[56] M. Boglione, J. Collins, L. Gamberg, J. O. Gonzalez Hernandez, T. C. Rogers, and N. Sato, Kinematics of current region fragmentation in semi-inclusive deeply inelastic scattering, Phys. Lett. B **766**, 245 (2017).

[57] L. Gamberg, A. Metz, D. Pitonyak, and A. Prokudin, Connections between collinear and transverse-momentum-dependent polarized observables within the Collins–Soper–Sterman formalism, Phys. Lett. B **781**, 443 (2018).

[58] S. Tafat, Nonperturbative corrections to the Drell-Yan transverse momentum distribution, J. High Energy Phys. 05 (2001) 004.

[59] A. A. Vladimirov, Self-contained definition of the Collins-Soper kernel, Phys. Rev. Lett. **125**, 192002 (2020).